Microscopy and Microanalysis, 2023, **00**, 1–13
https://doi.org/10.1093/micmic/ozad133

Microscopy AND Microanalysis

Original Article

On the Use of a Cluster Identification Method and a Statistical Approach for Analyzing Atom Probe Tomography Data for GP Zones in Al–Zn–Mg(–Cu) Alloys

Sohail Shah[1,*], Elisabeth Thronsen[2,3], Frederic De Geuser[4], Constantinos Hatzoglou[1], Calin D. Marioara[3], Randi Holmestad[2], and Bjørn Holmedal[1]

[1]*Department of Materials Science and Engineering, Norwegian University of Science and Technology (NTNU), N-7491 Trondheim, Norway*
[2]*Department of Physics, Norwegian University of Science and Technology (NTNU), N-7491 Trondheim, Norway*
[3]*SINTEF Industry, N-7465 Trondheim, Norway*
[4]*University Grenoble Alpes, CNRS, Grenoble INP, SIMaP, Grenoble F-38000, France*

***Corresponding author:** Sohail Shah, Email: sohailshah46@gmail.com*

Abstract

Early-stage clustering in two Al–Mg–Zn(–Cu) alloys has been investigated using atom probe tomography and transmission electron microscopy. Cluster identification by the isoposition method and a statistical approach based on the pair correlation function have both been applied to estimate the cluster size, composition, and volume fraction from atom probe data sets. To assess the accuracy of the quantification of clusters of different mean sizes, synthesized virtual data sets were used, accounting for a simulated degraded spatial resolution. The quality of the predictions made by the two complementary methods is discussed, considering the experimental and simulated data sets.

Key words: aluminum alloys, atom probe tomography (APT), Guinier-Preston (GP) zones, natural ageing (NA), pair correlation function (PCF), transmission electron microscopy (TEM)

Introduction

Atom probe tomography (APT) has a unique combination of three-dimensional (3D) spatial resolution down to the nanometer scale along with high chemical sensitivity (Kelly & Miller, 2007; Gault et al., 2012). This enables the study of small precipitates or clusters in metals. Quantification of cluster size and composition at different stages of precipitation is essential and remains at the forefront of research in understanding and designing the next generation of alloys.

Several approaches for cluster identification have been developed to define and characterize clustering and precipitation over the years (Johnson & Klotz, 1974; Vaumousse et al., 2003; Lefebvre et al., 2007, 2011, 2016; Stephenson et al., 2007; Gault et al., 2012; Samudrala et al., 2013; Miller & Forbes, 2014; Felfer et al., 2015; Hyde et al., 2017; Zelenty et al., 2017). In most cases, they consist of three data mining steps: (i) the clustering algorithm identifies solute clusters in the data by considering solute segregation, (ii) an enveloping algorithm searches for atoms of other elements that are within each solute cluster, and (iii) an eroding algorithm erodes the matrix–particle interface that may have formed as a result of the enveloping step.

These methodologies generally demand the user to manually determine multiple parameters, leading to inconsistent results and challenges in reproducing them. Also, to correctly identify certain clustering phenomena, a visual inspection of the results is often used to assess the accuracy of the parameters used. This too is strongly user dependent and can give inconsistent results. Usually, a well-defined parameter estimation procedure is used as seen for the case of the maximum separation method (MSM; Williams et al., 2013) to improve reproducibility and consistency in the results. Studying clustering and precipitation through atom probe is rendered more complicated due to the local magnification effects caused by differences in evaporation fields between different phases (matrix and particles; Vurpillot & Oberdorfer, 2015). The advantage of cluster identification is that it enables the extraction of local information, thus providing information on each identified cluster (composition, size).

Statistical approaches such as radial distribution functions (RDFs) (De Geuser et al., 2006; Sudbrack et al., 2006), on the other hand, aim at describing the distribution of solute atoms as a whole and do not consider each cluster separately. This gives element-specific averaged information on the cluster state of the matrix, both in terms of amplitude and correlation length. This enables a direct comparison of the degree of clustering between different data sets without the need of user-defined parameters.

Recently, Zhao et al. (2018) coupled a parameter-free statistical approach to an interpretation model enabling fitting of the RDFs in order to extract the composition of second-phase particles and estimate volume fraction, number density, and particle size. The methodology has previously been applied to Al–Cu–(Li–Mg) (Ivanov et al., 2017) alloys, the Al–Mg alloy system (Medrano et al., 2018), and the Al–Zn–Mg (Zhao et al., 2018) system. This enables a statistical significance of the results and reproducibility, while giving the average values from the data set analyzed.

Here, we combine two different approaches: a local cluster identification method, i.e., the isoposition method (IPM) and a

Received: August 14, 2023. **Revised:** October 26, 2023. **Accepted:** November 13, 2023

statistical methodology based on RDF or rather on pair correlation functions (PCFs; Lefebvre et al., 2016; Zhao et al., 2018). On the basis of these two methodologies applied to atom probe data sets of two Al–Zn–Mg–(Cu) alloys, as well as with the help of simulated data sets, we aim at better assessing the robustness of the experimental parameters obtained by APT on very small clusters.

Experimental Section

Six millimeter thick plates from two commercial alloys, received from Benteler automotives, were used in this study. The major difference between the two alloys is that one contains copper and is slightly richer in solute content, while the other is a copper-free alloy. The measured composition of the two alloys is given in Table 1.

Small blocks of samples sized 3 cm × 3 cm were cut and solution heat treated (SHT) at 480°C for half an hour in a salt bath followed by a water quench. The samples were grounded and polished for microhardness measurements using a 1,000 gf Vickers indenter. The hardness values reported are an average of five individual measurements for each condition. The alloys were naturally aged (NA) for 3 months at room temperature, after which they were characterized by APT and transmission electron microscopy (TEM).

All APT samples were prepared by following a standard two-step electropolishing process (Lefebvre et al., 2016). A minor contamination of copper (Cu) was seen as a capping layer at the tip of the APT needle similar as reported by Famelton et al. (2021). This could be due to the Cu present within the sample itself that contaminates the electrolytic solution (Danoix et al., 2001). The reconstructed volume containing this Cu-enriched region was removed from the subsequent data analysis.

APT experiments were carried out on a Local Electrode Atom Probe (LEAP) 5000XS from Cameca Instruments. It is a straight flight path instrument with a detection efficiency of 80%. For all analysis, the base temperature was set to 30 K, and the laser energy was adjusted to obtain an equivalent pulse fraction of 20% of the direct current voltage to avoid preferential evaporation (i.e., around 100–130 pJ; Hatzoglou et al., 2020). A detection rate of 0.5% and a pulse frequency of 250 kHz were used for all samples analyzed. Data sets containing 25–35 million ions were collected for each alloy. Reconstructions were made using the structural information according to Gault et al. (2009) by using the Integrated Visualization and Analysis Software (IVAS) by Cameca Instruments Inc. The Norwegian Atom Probe App software (2022) developed by C. Hatzoglou was additionally used for post processing of the experimental data and also to synthesize simulated data sets.

The cluster identification method used, i.e., the IPM method, was developed at the Groupe de Physique des Materiaux (University of Rouen, France) and is based on the chemical concentration (Mg + Zn) and an atomic distance criterion. A detailed explanation of the methodology and its criteria estimation can be found elsewhere (Lefebvre et al., 2016; Hyde et al., 2017).

Table 1. Measured Alloy Composition of the Investigated Alloys (Shah et al., 2022*b*).

		Cu	Fe	Mg	Si	Ti	Zn	Zr	Al
7003	wt%	0.01	0.22	0.73	0.09	0.02	5.68	0.15	Bal.
	at%	0.00	0.11	0.84	0.09	0.01	2.43	0.05	
7046	wt%	0.28	0.2	1.31	0.08	0.03	6.47	0.15	Bal.
	at%	0.12	0.1	1.52	0.08	0.00	2.79	0.05	

In the 7xxx Al alloy system, the clusters exhibit higher atomic density as compared to that of the matrix and with morphological distortion. This is mainly due to the local magnification effects typically caused by the difference in evaporation fields between cluster/matrix, previously reported (Hatzoglou et al., 2023, 2018; Lawitzki et al., 2021). The same local magnification effects have previously been reported in other studies (Shah et al., 2022*b*; Thronsen et al., 2023). However, the cluster dimension along the evaporation direction (Z direction) is less biased by local magnification effects (Vurpillot et al., 2000; Vurpillot & Oberdorfer, 2015), since it is the least biased direction in the APT. A more precise estimate of the size of clusters, as identified by IPM, can be based on a directional estimate in the Z direction, the so-called Extent$_z$ (E_z) parameter (Miller & Forbes, 2014), which for one cluster is defined as follows:

$$E_z = |Z_{\max} - Z_{\min}|. \quad (1)$$

Here, $Z_{\max}$ and $Z_{\min}$ are the outermost atoms in the Z direction of the identified cluster. Hence, E_z is the maximum distance between outermost cluster atoms in this direction. The E_z is comparable to how the diameter of spherical particles is typically measured from TEM images. Previous studies have found a correlation between the particle and tip size along with comparing APT and TEM size measurements (London et al., 2015). In this work, all APT data sets (7003 and 7046) started close to 3 kV, and the respective voltage history curves are given in the repository for tip size estimation.

Another standard way of estimating size for spherical particles in APT is using the radius of gyration (or diameter), as obtained from a cluster identification methodology. The radius of gyration is the root mean square of the distance between the center of mass and the coordinates of the constituent atoms classified as a cluster (Miller & Kenik, 2004; Lefebvre et al., 2016). Other methodologies like the best fit ellipsoid (Karnesky et al., 2007) can also be used to quantify size measurements for nonspherical particles but were not required in this study since the clusters in Al–Zn–Mg(–Cu) alloys are spherical (Lervik et al., 2021). Sizes reported in this study are all based on diameters extracted from the Guinier radius and from E_z. The Guinier diameter is simply twice the Guinier radius calculated from the cluster identification. The size and compositional errors are calculated based on the standard deviation. The error in the number density is calculated by dividing the number density with the square root of the total number of particles.

The PCF method is based on the RDF calculated for each solute (Zn, Mg, and Cu) as the central atom. The RDF $n_{a-b}(r)$ is defined as the number of atoms of species b at a distance r of an atom a. The RDF enables the computation of the average composition $C_{a-b}(r)$ of element b at a distance of r from the element a given as follows:

$$C_{a-b}(r) = \frac{n_{a-b}(r)}{\sum_b n_{a-b}(r)}. \quad (2)$$

If $\overline{C_a}$ is the bulk composition of element a, then in an isotropic system, $\overline{C_a}$. $C_{a-b}(r)$ is the correlation of the spatial composition of element a and element b given as follows:

$$\overline{C_a} \cdot C_{a-b}(r) = \langle C_a(\vec{r_1}) \cdot C_b(\vec{r_2}) \rangle. \quad (3)$$

where $r = |\vec{r_2} - \vec{r_1}|$. When r approaches large values (larger distances), the convolution approaches $\overline{C_a} \cdot \overline{C_b}$. The PCF can then be introduced by subtracting this final value:

$$\gamma_{a-b}(r) = \overline{C_a} \cdot C_{a-b}(r) - \overline{C_a} \cdot \overline{C_b}. \quad (4)$$

For large r, there is no correlation and $\gamma_{a-b}(r) = 0$. The PCF can be rewritten as follows:

$$\gamma_{a-b}(r) = \langle \Delta C_a(\vec{r_1}) \cdot \Delta C_b(\vec{r_2}) \rangle. \quad (5)$$

This highlights the fluctuation in composition ($\Delta C_a = C_a(\vec{r_1}) - \overline{C_a}$) and is relevant to the PCF. A normalized correlation function can further be introduced:

$$\gamma_{a-b}(r) = \Delta C_a \cdot \Delta C_b \cdot \gamma^0_{a-b}(r). \quad (6)$$

where $\gamma^0_{a-b}(0) = 1$ and $\gamma^0_{a-b} = 0$ for large r. If we consider only a single type of ion, we obtain the autocorrelation:

$$\gamma_{a-a}(r) = \Delta C_a^2 \cdot \gamma^0_{a-a}(r). \quad (7)$$

As mentioned by Zhao et al. (2018), the mean squared composition fluctuation is immune to the local magnification effects due to difference in the electric field required to induce the evaporation phenomenon of the different phases (but not to spatial resolution effects).

If we further assume a two-phase system with a homogenous composition of element a, with precipitate composition C_p^a in a matrix of composition C_m^a and that both share the same atomic volume, the volume fraction f_v of the precipitates can be written as follows:

$$f_v = \frac{\overline{C_a} - C_m^a}{C_p^a - C_m^a}. \quad (8)$$

The average of the product of compositional fluctuations can then be calculated as follows:

$$\overline{\Delta C_a \cdot \Delta C_b} = f_v(1 - f_v)(C_p^a - C_m^a)(C_p^b - C_m^b). \quad (9)$$

For a single type of ions, this can be simplified as follows:

$$\overline{\Delta C_a^2} = f_v(1 - f_v)(C_p^a - C_m^a)^2 = (C_p^a - C_a)(C_a - C_m^a). \quad (10)$$

The PCF value at the origin ($r = 0$), when considered alongside the matrix composition (Geuser & Lefebvre, 2011), offers a robust means of extracting precipitate composition and volume fraction, free from the influence of local magnification effects. The normalized correlation function for a sphere of radius R can also be calculated assuming a homogenous density with a sharp interface with the matrix as follows (Guinier et al., 1955; Philippe et al., 2009):

$$\gamma_0^{\text{sphere}}(r, R) = \begin{cases} 1 - \frac{3r}{4R} + \frac{r^3}{16R^3} \ (r \le 2R) \\ 0 \ (r > 2R) \end{cases}. \quad (11)$$

Assuming a log-normal size distribution of spheres and integrating Equation (11), the experimental data can be fit to extract the size of the clusters. A 20% dispersity in the log-normal distribution is assumed, and a contribution of an excluded volume is also added (Kruglov, 2005).

The PCF is plotted as $\gamma(r) \cdot r$, allowing for an easier comparison of the differences in size between different conditions, since the position of the maximum of $\gamma(r) \cdot r$ is related to the length of correlation (i.e., to the size of the clusters).

The TEM specimens were prepared by grinding bulk specimens to ~100 μm thickness before they were punched out to 3 mm disks and subsequently electropolished using an electrolyte mixture of 1/3 HNO_3 and 2/3 C_3CH_3OH. The temperature was kept at 25 ± 5°C at an applied voltage of 20 V. High-angle annular dark-field scanning TEM (HAADF-STEM) images were collected using a double-corrected JEOL ARM200CF operated at 200 kV with convergence semiangle and inner collector angle 27 and 48 mrad, respectively.

Results

Hardness

The hardness of the supersaturated solid solution (SSSS) for the 7003 alloy starts at around 46 HV while it is higher for the 7046 alloy, close to 61 HV. The hardness progressively increases for both alloys during NA, as shown in Figure 1.

The hardness measurements taken after 3 months of NA revealed a considerable hardness increase to around 115 HV for the 7003 alloy and 135 HV for the 7046 alloy. Further hardness measurements revealed that the hardness for both alloys later saturated at around 125 and 155 HV for the 7003 and 7046 alloy, respectively, after 1 year NA. Nevertheless, 3 months of NA was chosen as the conditions to characterize the microstructure of these alloys.

APT Results Processed by the IPM Methodology

The APT data sets were used to extract smaller regions of interest (ROI) that were used for visualizing the clustering, as shown through Figures 2a and 2b for 7003 alloy and Figures 2d and 2e for 7046 alloy. The IPM was used to extract size distributions, as seen in Figures 2c and 2f for 7003 and 7046 alloys, respectively. Size measurements in this study refer to the diameter of the precipitates measured using Equation (1) similar to our previous studies (Shah et al., 2022*a*, 2022*b*). Additionally, the radius of gyration has been used to elucidate the mean diameter. The radius of gyration is the radius of a body having its mass concentrated at a single distance from its center of mass (Kelly & Miller, 2007; Gault

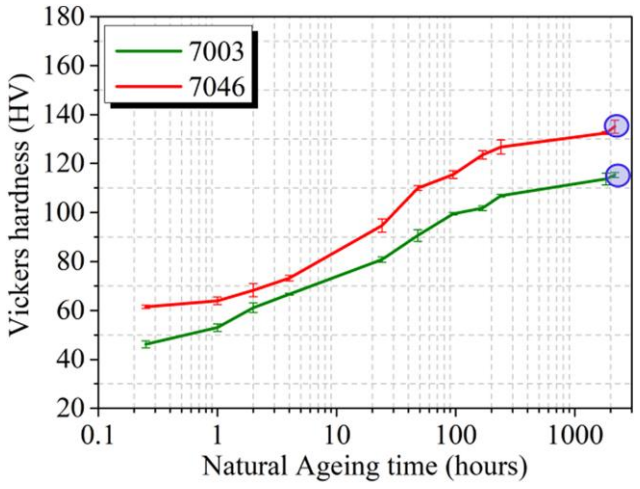

Fig. 1. Evolution of hardness as a function of ageing time for both 7003 and 7046 alloys. The blue circles indicate the condition that was chosen for APT analysis.

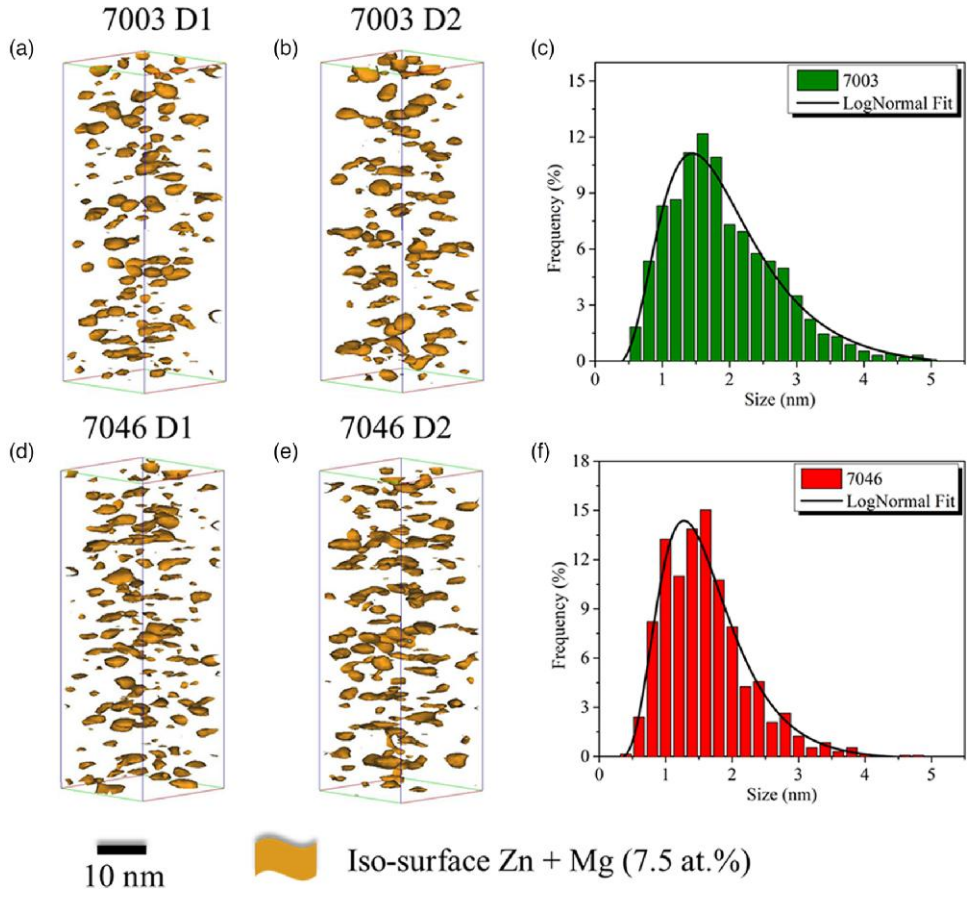

Fig. 2. APT subvolumes of dimensions $25 \times 25 \times 70$ nm^3 extracted from the APT data sets showing clustering in the 7003 alloy for (**a**) data set 1 and (**b**) data set 2. Similar cluster volumes for the 7046 alloy are shown for (**d**) data set 1 and (**e**) data set 2. The average size distribution based on E_z of the two data sets of the two alloys is shown in (**c**) and (**f**).

et al., 2012). The size distributions shown are an average of the size distributions obtained for the two data sets for each alloy.

For both alloys, the size distribution fits well with a log-normal distribution. Table 4 shows the quantitative measurements extracted from the IPM. It is quite evident that the two data sets for each alloy show similar size and composition of the clusters. The average size of the clusters for the 7003 alloy is around 1.8 nm, while it is slightly lower, around 1.5 nm, for the 7046 alloy, as measured by E_z. The average Zn/Mg ratio for the 7003 alloy is around 2 while it is around 1.5 for the 7046 alloy, as indicated in Table 4. The measured Extent$_x$ (E_x) is consistently larger than E_z, as seen in Table 2 for all four data sets whereas the opposite is expected for low-field particles. This is mainly due to the spatial resolution aspect of APT dominating the local magnification effects and will be discussed in the Discussion section. Since Extent in x and y are very similar, only E_x is reported in Tables 2 and 4. The measured E_z is in close agreement with the size measurements by TEM (shown in the Cluster Observations by HAADF-STEM section) and hence is regarded as more relevant in terms of describing the size using the IPM in this case.

APT Results Processed by the PCF Methodology

The calculations of zinc (Zn–Zn), magnesium (Mg–Mg), copper (Cu–Cu) correlations along with the cross correlations for the three elements are shown in Figure 5. The first maximum of the curves, indicative of the size of the objects, is similar for all the correlations. This indicates a single distribution of clusters containing both Zn and Mg (and Cu for 7046). This size is consistently smaller for 7046 than for 7003, in agreement with the IPM results. The amplitude of the Zn–Zn PCF is larger for 7003 than for 7046, while the Mg–Mg PCF amplitude is smaller for 7003 than for 7046. These observations confirm a higher Zn/Mg ratio for the 7003 than for the 7046. The Cu correlations in Figure 3 are shown only for the 7046 alloy, since 7003 is a Cu-free alloy. Figure 3f shows higher scatter for the Cu–Cu plot due to lower signal from the Cu atoms.

More quantitative results can be obtained from the PCF by fitting the data to a two-phase modeled data set (matrix + clusters) containing spherical particles of homogeneous composition and with sharp interfaces (we shall further see that while this might be a reasonable assumption for larger precipitates, it is a coarse approximation for small clusters). The spherical shape is a good approximation being confirmed by the TEM analyses presented in the Cluster Observations by HAADF-STEM section. We further assume a log-normal distribution of the diameter. This model implies that all correlations should be proportional, i.e., they should all have the same shape $\gamma_0(r)$ but with a different amplitude $\overline{\Delta C}^2$. For more efficient fitting, we thus fitted the shape to the Zn–Zn correlation and assumed it was fixed for the other correlations, with only the amplitude changing. Despite the limitations of the interpretation model (spheres, homogeneous composition,

Table 2. Average (Mean) Results of Cluster Analysis by IPM for APT Data Sets of 7003 and 7046 Alloys.

	Mean Diameter (nm)	E_x (nm)	E_z (nm)	Cluster Composition (at%)			Number Density (10^{24}/m^3)	Zn/Mg
				Zn	Mg	Cu		
7003 D1	2.45 ± 0.60	2.59 ± 1.53	1.75 ± 0.91	11.77 ± 0.32	5.82 ± 0.22	0.09 ± 0.02	3.19 ± 0.08	2.03 ± 0.14
7003 D2	2.53 ± 0.59	2.69 ± 1.45	1.88 ± 0.84	10.77 ± 0.29	5.35 ± 0.21	0.04 ± 0.01	3.25 ± 0.08	2.02 ± 0.10
7046 D1	2.15 ± 0.45	2.29 ± 1.10	1.50 ± 0.64	11.59 ± 0.41	7.61 ± 0.15	0.19 ± 0.10	2.34 ± 0.07	1.52 ± 0.08
7046 D2	1.96 ± 0.39	1.63 ± 1.02	1.21 ± 0.57	12.39 ± 0.45	8.09 ± 0.67	0.32 ± 0.19	1.51 ± 0.10	1.54 ± 0.17

The uncertainties are calculated through $2\sqrt{\frac{C(1-C)}{N}}$, where C is the concentration of a particular element and n the total number of atoms in the isolated clusters identified by IPM.

Table 3. Mean Cluster Size (Diameter), Composition, Number Density, and Zn/Mg Ratio Obtained by Fitting the PCF Methodology Data in Figure 5 Assuming a Log-Normal Distribution of Spherical Clusters.

	Mean Diameter (nm)	Cluster Composition (at%)			Number Density (10^{24}/m^3)	Zn/Mg
		Zn	Mg	Cu		
7003 D1	2.98	9.76	5.03	0.14	5.9	1.97
7003 D2	3.15	8.69	4.52	0.11	6.3	1.95
7046 D1	2.61	7.76	5.34	0.3	13.2	1.47
7046 D2	3.1	8.02	5.32	0.36	7.7	1.53

and sharp interface), the quality of the fit is excellent, enabling the parameters of the model (size, compositions) to be extracted.

The parameters extracted from the fit are shown in Table 3. These parameters show similar trends as the results from IPM, i.e., the clusters in 7003 are consistently larger than in the 7046 and the cluster compositions are in reasonable agreement with the Zn/Mg ratio being close to 2 for 7003 and 1.5 for 7046. The main source of uncertainties on the values obtained through fitting is not due to the fitting procedure itself but rather to the limitation of the fitting model itself, i.e., a distribution of spheres with homogenous composition and a sharp interface with the matrix. The effects of these limitations on the parameter values are difficult to quantify but will be further discussed in the Discussion section. There are also systematic discrepancies between the IPM and PCF results, which can be explained by the way these parameters are computed and will be discussed further in the Discussion section.

Cluster Observations by HAADF-STEM

Atomically resolved HAADF-STEM was employed to investigate the clusters in the alloys. Figures 4a and 4b show that both 7003 and 7046 exhibit a dense population of Guinier Preston (GPI) zones. Visually, the GPI zones have a larger diameter in the 7003 alloy. This is in accordance with our previous results on the same alloy (Shah et al., 2022*b*). To investigate this in a quantitative matter, the diameters of at least 300 GPI zones were measured per condition. The GPI zones in 7003 had an average diameter of 1.87 ± 0.17 nm, while in 7046, the average diameter was 1.67 ± 0.11 nm. The E_z is very similar to the way size measurements from TEM results often are obtained. In this work, the size measurements of the GPI zones in the STEM images were estimated by assuming that the zones were spherical in shape. For each zone exhibiting clear atomic structure, the size was estimated by measuring the diameter of the zone. The error is given as the standard deviation.

The size distributions of alloys 7003 and 7046 are illustrated in Figures 4c and 4d. In this analysis, we focused on estimating the distribution using only the structured GPI zones that were clearly identifiable, encompassing approximately 50–60 GP zones. The inclusion of unstructured clusters, typically those with diameters smaller than 1 nm, posed a challenge due to the uncertainty of their overlap with lower-lying clusters. It is important to note that while this limitation should not significantly impact the observed trend, which indicates slightly larger clusters in the 7003 alloy compared to the 7046 alloy, it does imply that the mean diameters estimated from HAADF-STEM are likely to be overestimated.

The IPM and the PCF Methodology Applied on Simulated Data Sets

Experimental artifacts associated with an APT data set include the following:

(i) A detection efficiency of 80% (similar to the LEAP 5000XS used to analyze the experimental data sets in Fig. 2).
(ii) Positioning uncertainty of atoms with different resolutions.

The reduced detection efficiency of 80% was accounted for in the simulated data sets. APT volumes were simulated with box dimensions $20 \times 20 \times 100$ nm^3. A data set with a mean particle diameter of 1.8 nm was synthesized, picked up from the learnings of the 7003 alloy data sets. This is labeled as V1.8. A standard deviation of around 20% of the mean diameter and a log-normal distribution were applied. The particles were Zn and Mg enriched but without Cu, like the experimental data sets of the 7003 alloy. Only Al, Zn, and Mg elements were used to generate the volumes. The particles introduced into the volumes had a sharp interface. Once all particles have been introduced, a random spatial distortion of each atom position was made to obtain a more realistic data set as compared to an experimental measurement. Hence, the initially abrupt particle interface was blurred.

First, an "ideal resolution" of 0.2 nm in depth and 0.5 nm in lateral resolution was applied to the entire data set. This is a Gaussian resolution with 0.2 and 0.5 nm representing 2σ. This implies that the position of atoms was randomized by 0.2 and 0.5 nm in the evaporation and lateral directions, respectively. The concentration of solute in the particles is set higher than what is extracted from the experimental data. This is done in order to try and simulate the experimental data with respect to particle metrology. Next, the resolution is degraded until a match in the PCFs is observed when compared with the experimental PCFs. We call this dataset the "degraded resolution" and label it V1.8DR.

The number densities of both data sets were set to $1E^{25}$ m^{-3}. The size distribution for V1.8 is shown in Figure 5b while the

Table 4. Average (Mean) Results of Particle Analysis Done by the IPM on Simulated Volumes.

Condition	Guinier Diameter (nm)	E_x (nm)	E_z (nm)	Cluster Composition (at%) Zn	Mg	Number Density (10^{24}/m^3)	Zn/Mg
V1.8	2.32 ± 0.24	2.36 ± 1.11	2.24 ± 1.01	16.56 ± 0.52	8.17 ± 0.32	5.65 ± 0.02	2.03 ± 0.08
V1.8DR	1.93 ± 0.20	2.40 ± 1.012	1.89 ± 0.86	12.92 ± 0.37	6.37 ± 0.21	3.50 ± 0.01	2.03 ± 0.07

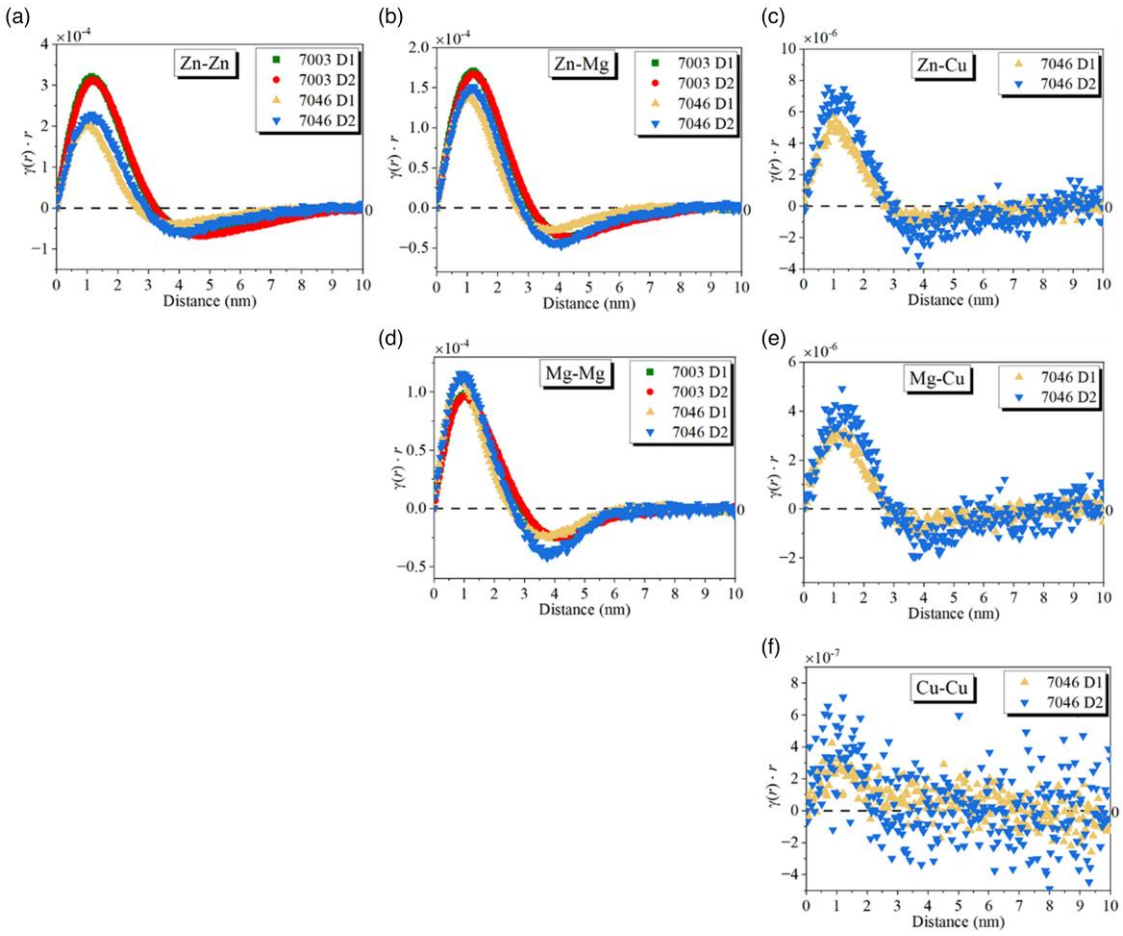

Fig. 3. Pair correlation functions for (**a**) Zn–Zn, (**b**) Zn–Mg, (**c**) Zn–Cu, (**d**) Mg–Mg, (**e**) Mg–Cu, and (**f**) Cu–Cu pairs from the APT data sets shown in Figure 2.

corresponding PCFs are seen through Figures 5c–5e. The amplitude of the PCF of V1.8 is much greater than other data sets (experimental and simulation) while the amplitude of PCF of V1.8DR is very similar to that of the experimental data sets (7003 D1 and D2).

The quantitative data extracted by the IPM for V1.8 and V1.8DR are shown in Table 4. Both these volumes have a higher concentration of solute input in the particles; 20 at% Zn and 10 at% Mg. Since both the ideal resolution and the degraded resolution volumes resulted in concentrations much lower than the input concentrations, it is clear from the IPM results that the apparent composition of the clusters is greatly affected by the resolution. Number densities of detected clusters are also highly affected, for both volumes, as seen in Table 4.

When the resolution is degraded, the size measurements for V1.8DR by the IPM are underestimated, as seen in Table 4, using the E_z parameter, being smaller than expected. This is a nontrivial effect, which indicates that a substantial proportion of the interfacial cluster atoms has been attributed to the matrix during IPM. Since the applied spatial resolution is better in Z than in XY, the E_x values are consistently larger than E_z.

Because of the broader extension of the clusters due to the spatial resolution, the PCF methodology computes a larger average size than prescribed by the input data set. The degraded resolution also strongly affects both the number of detected solutes in the clusters and their number densities, cf., Tables 4 and 5.

The PCF methodology confirms the effect of the degraded resolution with similar results as compared to IPM for V1.8, as seen in Tables 4 and 5. Most importantly, it should be noticed that V1.8DR seems to mimic the behavior of the 7003: it gives similar results on the detected clusters with both IPM and PCF, the overall shape and amplitude of the PCF curves are similar, and the volume was obtained with initial cluster sizes compatible with HAADF-STEM.

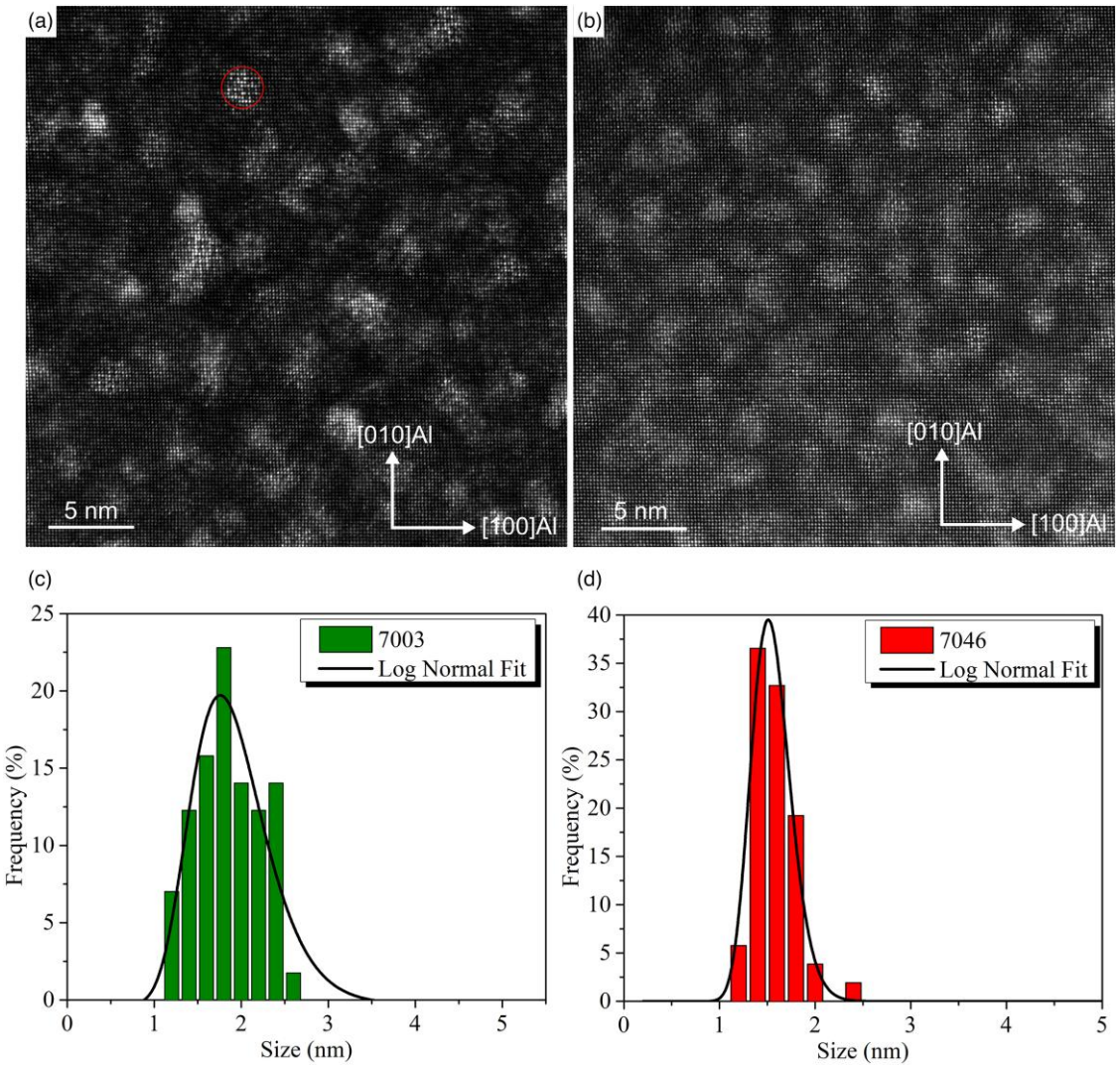

Fig. 4. HAADF-STEM images from (**a**) 7003 and (**b**) 7046 showing a dense population of GPI zones. The red circle in (**a**) exemplifies how the sizes of the GPI zones were estimated using the diameter of the circle. Corresponding size distribution estimation has been done for (**c**) 7003 and (**d**) 7046 based on 50–60 clusters. The finer clusters without structure were not included in the statistics due to uncertainty of overlap.

Discussion

The Apparent Discrepancies in the Cluster Parameters as Seen by the Methodologies

We have looked at the clustering state in the 7003 and 7046 alloys by APT (IPM and PCF) and by HAADF-STEM. We found similar trends among the methods: the clusters seem consistently smaller in the 7046 than in the 7003. The Zn/Mg ratio was found to be about 2 for 7003 and 1.5 for 7046 with both APT methods. There are however systematic discrepancies that can be at least partially explained both by the difference in approach between IPM and PCF based methods and by the nature of APT data. These discrepancies are as follows:

(i) The IPM method finds consistently higher solute content in the clusters than the PCF methodology.
(ii) The IPM method finds consistently lower number density of clusters than the PCF methodology.
(iii) Both APT methods find larger clusters than HAADF-STEM.

These discrepancies should be discussed in the context of very small clusters that do not present a sharp interface with the matrix, partly or entirely because of a finite spatial resolution limiting the positioning accuracy.

It should be kept in mind that the IPM methodology and the PCF methodology are two very different approaches. The IPM is a cluster identification method. Its objective is to label each atom in the data set as belonging either to the clusters or to the matrix. The result depends on the choice of parameters, which are chosen through an optimization process aiming at minimizing the amount of "false positives" whereby atoms from the matrix are wrongly labeled as clusters. It requires as input an estimate of a minimal size for the clusters. An erosion step guarantees that the clusters do not include a shell of matrix. This ensures that compositions computed on the detected clusters are measured in a condition, neither including too small clusters nor interfacial area of the clusters that includes matrix atoms from a diffuse interface.

This is in contrast with the PCF method, which considers the data set as a whole and assumes that the clusters have a homogeneous composition. Hence, when the cluster/matrix

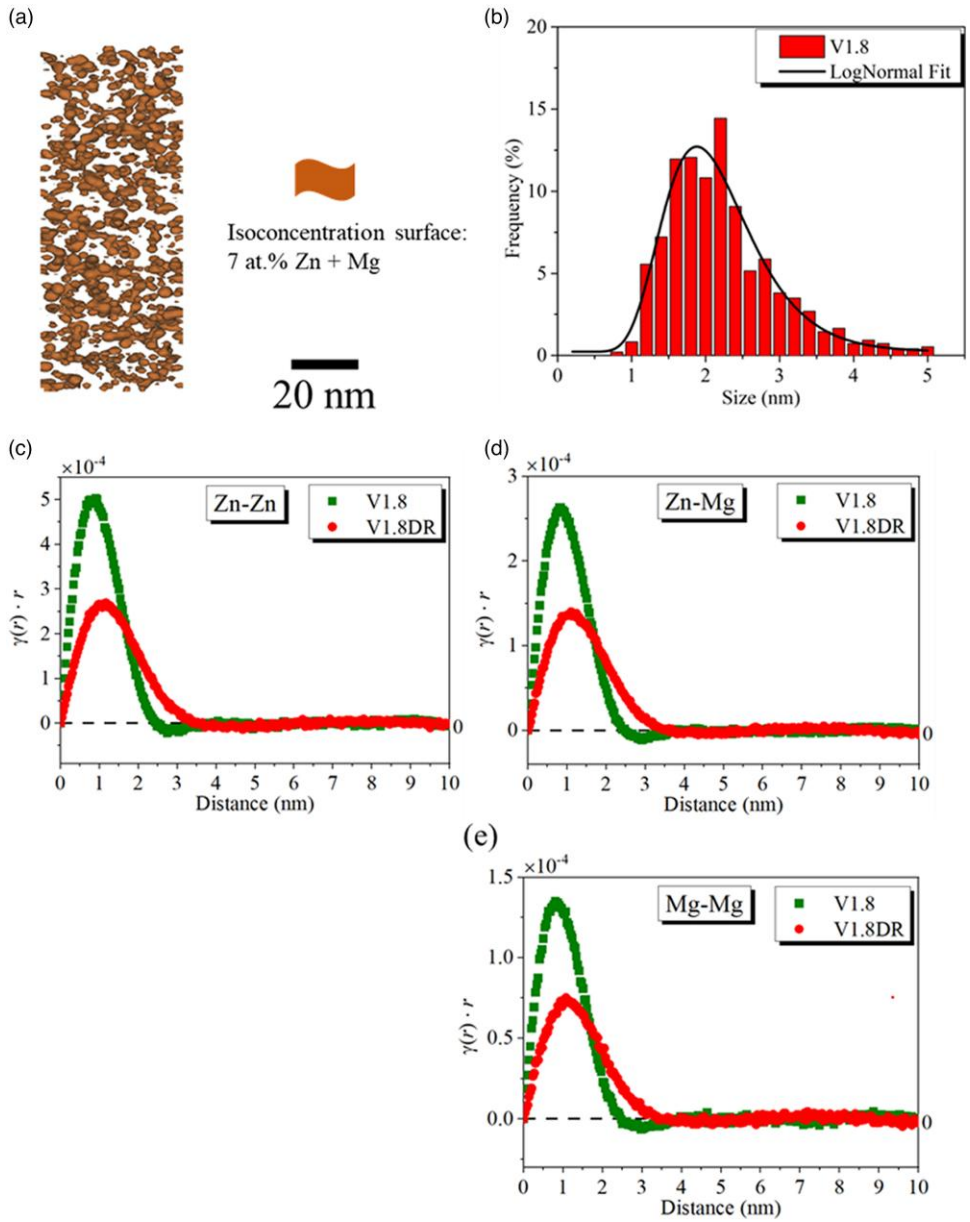

Fig. 5. Simulated volume (**a**) V1.8 showing isoconcentration surface of 7 at% Zn + Mg to visualize the particles inserted. Size distribution obtained from IPM for (**b**) V1.8. PCF for (**c**) Zn–Zn, (**d**) Zn–Mg, and (**e**) Mg–Mg for both volumes.

interface is actually diffuse and the cluster size is small, the average composition measured by the PCF fitting method is likely to be smaller, explaining discrepancy (i).

Discrepancy (ii) is indirectly related to (i) and can also be explained by the selective approach (IPM) versus global approach (PCF): the smaller clusters from the data set may be part of the cluster distribution fitted by the PCF approach while being labeled as too small to be a cluster by IPM, thus lowering the detected number density. Whether this is a good or a bad thing depends on the situation. The IPM parameters could be set to detect more clusters but very likely at the cost of an apparent lower cluster composition.

Discrepancy (iii) is more informative on the metrology of such small clusters by APT than on the methods themselves. The size histograms obtained by HAADF-STEM are likely to be very good estimates of the size of the clusters. If anything, they might be slight overestimations since the smaller diffuse clusters were left out of the calculation. This means that the clusters' apparent size in APT is too large. Since the data set reconstructions were properly calibrated and since the local magnification effect (higher density in these objects) should have a reverse effect, this can be only attributed to a spatial resolution blurring of the interfaces (De Geuser & Gault, 2020).

The application of the two methodologies to simulated data sets enabled to better estimate the instrumental effect on the cluster parameters by attempting to create realistic simulated data sets that are compatible with our experimental results.

Studies of Simulated Volumes

Number Density Measurements

From the ideal resolution data set, 64% of the particles are detected with the IPM, while when applied to the degraded

Table 5. Mean Particle Diameter, Composition, Number Density, and Zn/Mg Ratio Obtained by the PCF Methodology by Fitting the Data in Figure 5, Assuming a Log-Normal Distribution of Spherical Particles.

Condition	Diameter (nm)	Particle Composition (at %)		Number Density (10^{24}/m^3)	Zn/Mg
		Zn	Mg		
V1.8	2.24	18.76	9.43	6.82	1.99
V1.8DR	2.90	10.50	5.12	5.14	2.05

resolution data set (V1.8DR), only 39% of particles are detected. Hyde et al. (2017) found it challenging to detect clusters smaller than 1 nm in diameter using the same methodology, while the detection of clusters was even worse using the MSM, despite having a higher solute concentration contrast between the matrix and the clusters. This is in line with the current observations as demonstrated in Figure 5b with the size distribution showing no clusters detected below 1 nm in diameter.

The results for the "degraded resolution" suggest that the number densities measured are even lower when a lower resolution is accounted for. The spatial distortions in lateral and depth resolution make it further challenging to detect the clusters smaller or close to 1 nm in diameter. To distinguish the smallest particles (with diameter smaller than about 1 nm) from random solute fluctuations becomes problematic, and thus, a lot of fine particles are not detected by the IPM. With the methodology estimation reported by Hyde et al. (2017), no false-positive clusters were introduced. This was done by comparing the "real cluster id" generated from the simulated volume with the IPM cluster id. With the degraded resolution, the smaller clusters are simply not there anymore due to the blurring caused by the spatial resolution effects.

The statistical method using the PCF, on the other hand, estimates the number density from the volume fraction of particles based on the average volume of particles as $f_v/\langle V\rangle$. There is only a slightly higher estimated volume fraction for the cases with degraded resolution. However, the average particle diameter estimated for V1.8DR is higher than for V1.8. Hence, similar number densities are predicted by the PCF methodology for the ideal resolution and the degraded spatial resolution. As already discussed, this difference between IPM and PCF is due to different approaches (selective for IPM and global for PCF).

Size Measurements

When considering the ideal resolution data set (V1.8), we see that both methods (IPM and PCF) overestimate the size of particles by around 28%, cf., Tables 4 and 5. However, when considering the degraded resolution data set (V1.8DR), a smaller average cluster diameter is estimated by the IPM (~1.9 nm, cf., Table 4), while the PCF methodology overestimates the size by almost 60% (cf., Table 5). The IPM mitigates the effect of spatial resolution and blurring of atoms by utilizing the erosion step, which removes the interface atoms from the clusters. This in turn reduces the size of clusters and can explain the trend of lower size measurements for V1.8DR. Note that this data set is very similar to the experimental one in terms of PCF amplitudes and concentration estimates.

The PCF methodology, on the other hand, slightly overestimates the cluster diameter with degraded spatial resolution. This can be explained by the scatter to the atomic positions, which for the PCF methodology leads to an increase in the net volume within each cluster. The volume fraction measured by the PCF methodology also increases for V1.8DR as compared to their ideal resolution counterparts, which explains the increase in the mean diameter estimated by the PCF methodology.

Composition Estimates

The simulated volumes V1.8 and V1.8DR had a higher input concentration of solutes in the particles (Zn = 20 at% and Mg = 10 at%) than the measured ones. This was mainly done to achieve a similar amplitude of the PCFs after spatial degradation as compared to the experimental data. The amplitudes of V1.8DR and of the experimental data set (7003 D1 and D2) are very similar, as seen in Figure 6.

For both the IPM and the PCF methodology, the Zn and Mg contents in the clusters are close to the input composition of particles for V1.8. However, when the spatial resolution is degraded, the Mg and Zn contents in the clusters become underestimated by both methodologies for V1.8DR, as seen in Tables 4 and 5.

Let us first consider the PCF approach. The amplitude of PCFs for the degraded data sets is smaller than its ideal resolution counterpart, as seen in Figure 6. Note that Equation (10) for the particle compositions involves the bulk composition as well as the matrix composition. C_p^a is very sensitive, because of the factor of $1/(\overline{C} - C_m)$ being close to zero in Equation (10). This increases the uncertainty and makes the composition of solute in particles challenging to accurately measure by this method. The computation of the particle composition thus strongly depends on the matrix and bulk compositions used. The values of ΔC^2_{Mg}, ΔC^2_{Zn} and $\Delta C^2_{\mathrm{Zn-Mg}}$ at $r = 0$ can be used in Equation (10) to extract these as the two unknowns (C_p^{Mg} and C_p^{Zn}), although matrix compositions can be influenced strongly by the lateral scatter.

Although IPM estimated the composition of particles in V1.8 close to the input concentrations, care must be taken, since the particles smaller than about 1 nm in diameter remain undetected due to the spatial degradation and possibly the particles no longer existing (become a part of the random fluctuation). These small particles then become poorly represented in terms of the statistics. Hence, the composition of these particles has a high uncertainty, and the estimated composition is dominated by the larger particles, which have a defined interface and composition. However, in the synthesized samples considered here, all particles had the same stoichiometry; hence, this issue did not affect the estimates in our cases.

The IPM underestimates the composition for the degraded resolution volumes. This is expected, since the lateral scatter can result in the artificial introduction of a significant level of matrix (Al) into the defined particle. A similar trend was seen by Hyde et al. (2011) when using MSM to determine the composition for simulation of trajectory aberrations. This results in a small solute cluster being significantly diluted due to the scatter caused by the degraded resolution parameters.

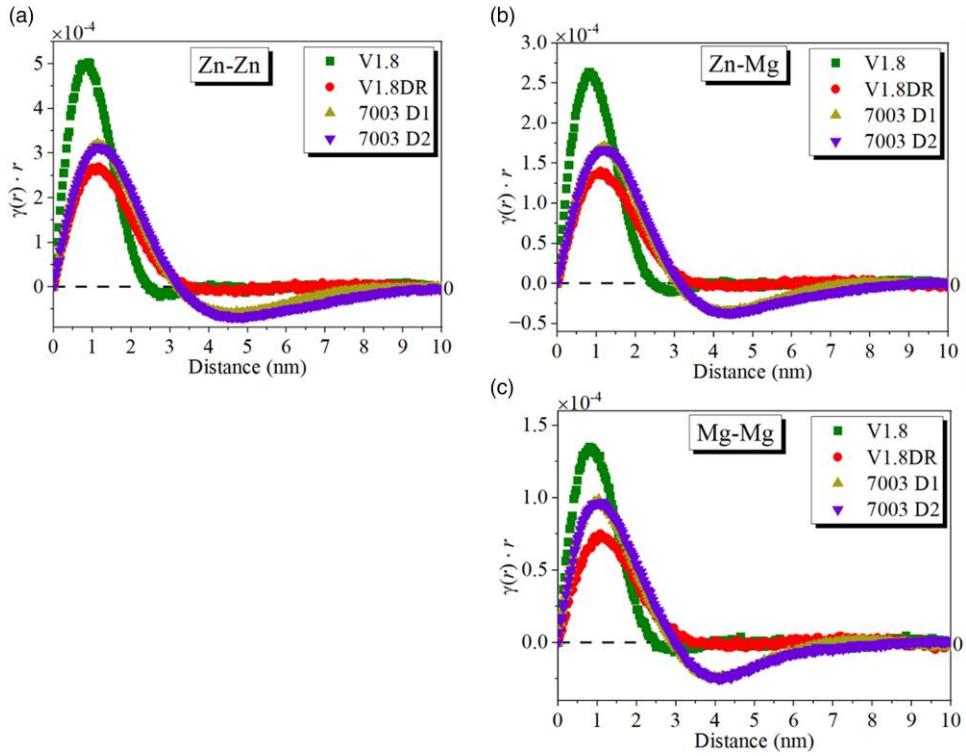

Fig. 6. PCF plots of (**a**) Zn–Zn, (**b**) Zn–Mg, and (**c**) Mg–Mg for the simulated and experimental (7003) data sets. The degraded resolution data set of the simulated volume is a close match in terms of PCFs compared to the 7003 data sets.

Interestingly, the concentration of solute in particles measured by both IPM and PCF for V1.8DR is very similar to the experimental data sets, as seen in Table 3. Although the solute concentration is underestimated when compared to the input values in the data set, we see that the degraded resolution (V1.8DR) is indeed a good representation of the actual experimental data set. This in turn indicates the underestimation of solute concentration in the experimental data sets. It is well known that the local magnification effects cause trajectory aberrations, coupled with degradation of resolution ultimately leading to the underestimation of solute inside particles. We see a similar trend here confirmed by V1.8DR, wherein a higher concentration of solute in particles is heavily underestimated, causing erroneous composition measurements. The Zn/Mg ratio estimated for both simulated volumes is close to 2, as seen from Tables 4 and 5, indicating that the quantification of the amount of Zn and Mg inside particles is affected proportionally, and hence, the true ratio is expected to be preserved.

Experimental Data Interpretation

The analysis conditions were optimized for the experimental data to avoid preferential evaporation. A high pulse fraction and low temperature were used to analyze all data sets (Saxey, 2011). No sign of molecular dissociation (Jin et al., 2022) was seen. Based on the understanding gained from the simulated volumes, the average compositions of GP zones for 7003 and 7046 alloys estimated by both PCF methodology and IPM are underestimated. The apparent particle composition was lower than the input value (20 at% Zn and 12 at % Mg) for the simulated volume, along with a reduced measured number density, mainly due to particles below 1 nm not being detected.

In principle, the shapes of the PCFs for Zn, Mg, and Zn–Mg should all be the same, since they originate from the same particles (spheres). This is very well reproduced in the simulated volume, as seen in Figures 5b and 5c. Both simulated volumes (V1.8and V1.8DR) have the same shape as seen from Figures 5b and 5c. They overlap each other and follow the "pseudo-binary" assumption.

The experimental data set, on the other hand, shows slightly different shapes of the PCFs. Since we have only a single population of clusters (GP zones predominantly), we should ideally expect all PCFs to be of the same shape. In particular, the mean size of the GP zones would be slightly smaller if it was based on the fit from Mg rather than that of Zn. Several works on Al–Zn–Mg alloys (Stiller et al., 1999; Engdahl et al., 2002) have reported this effect, where the extension of the Zn enrichment in precipitates is higher than that of Mg. This can be interpreted as an APT artifact, wherein subtle changes in the evaporation field of the matrix atoms within particles change the electric field distribution and hence cause these chromatic aberrations (Marquis & Vurpillot, 2008).

However, the use of the Zn PCF in the calculations cannot solely explain the overestimation of the mean diameter by the PCF methodology. A decrease of the estimated diameter of around 7% is seen when using the PCF of Mg instead of Zn. The spatial resolution is element specific, as we see in the case of PCFs plotted for different elements for the same data set in Figure 7. This is more of an instrument effect that is not seen in the simulated volumes. Additionally, this will also affect the results obtained by the IPM. The spatial resolution plays an important role in determining the size, as also pointed out by other authors (Marquis & Vurpillot, 2008; De Geuser & Gault, 2020).

It can be seen by comparing Figure 6a and Figures 5b and 5c that there is a part of the PCF that is negative. This "dip" is

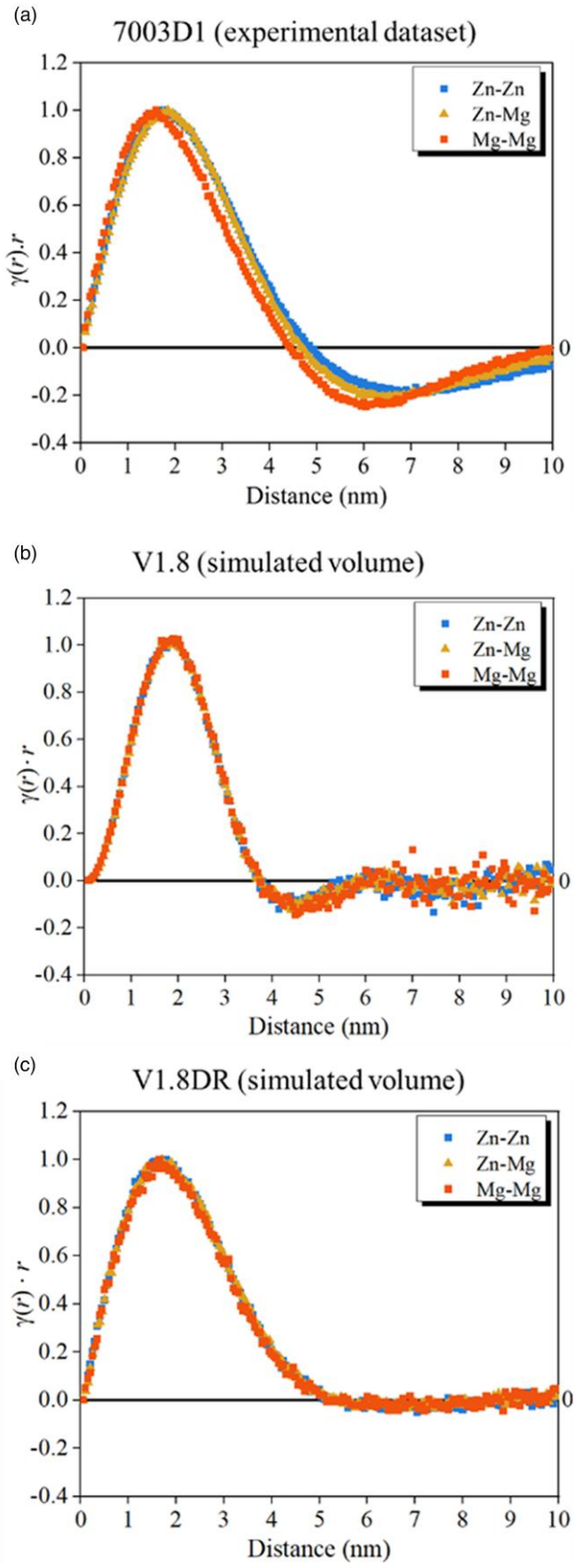

Fig. 7. Normalized PCF for Zn–Zn, Zn–Mg, and Mg–Mg obtained from (**a**) 7003 experimental data set and simulated volumes (**b**) V2DR and (**c**) V3DR.

more prominent in the PCF curves from the measured experimental data sets than in the simulated volumes. The interparticle interaction qualitatively gives this effect, and the dip can be well reproduced by accounting for an "excluded volume" (Kruglov, 2005) in the PCF methodology. This is because two particles cannot overlap. Hence, the position of each particle is not independent. However, the dip can also be due to depletion in solute around the particles as part of the solute diffusion, which is also not accounted for. Anyhow, the correction for the dip decreases the estimate of the mean diameter only slightly, by a few percent. Hence, it will neither affect much the estimates of particle compositions.

The IPM gives representative size measurements with Guinier diameter, E_x, and E_z for the simulated volumes as seen in Tables 4 and 5. This is not the case for experimental data sets though. TEM measurements agree with the IPM size measurements (E_z) for the experimental data sets. The E_x is overestimated for all four data sets and on average is around 1.7 times the E_z. The considered clusters are low-field precipitates giving rise to higher atomic density; hence, the opposite was expected, i.e., a contraction in the XY plane and potentially to appear smaller. However, this is not the case. This opposite trend is attributed to the local magnification effects and trajectory overlaps due to the difference in evaporation field between the matrix and particles, which are seen in the experimental data sets (Vurpillot et al., 2000). In other words, the spatial resolution is locally worse.

Number density measurements, as highlighted in the above section, are heavily underdetermined by IPM for V1.8. From the TEM results, many disordered clusters smaller than 1 nm are seen, which are not taken into account while estimating the size distribution as seen in Figures 4c and 4d due to the challenge of deconvoluting the overlapping clusters.

Both methodologies have shown reasonable agreements on size and composition measurements. The important understanding from the simulated volumes in an attempt to mimic the experimental data sets showed that both methodologies underestimate the concentration of solute within particles. Features less than 1 nm usually go undetected, and consequently, the number densities are underestimated. Care must be taken, since number densities measured by IPM are sensitive to the size of the particles, while the estimate by the PCF is based on the average volume of the particles.

Conclusions

By using a combination of APT data interpretation methodologies, supported by simulated data sets and HAADF-STEM experiments, we have shown that reliable APT measurements of the size and compositions from small clusters issued from the early stages of decomposition in Al–Zn–Mg alloy are challenging. Because of their small size, the particles/clusters are subject to significant distortions due to degraded resolution, leading to an increase of their apparent size as well as a decrease of their apparent solute content. While these effects are likely to be system dependent, we have estimated in our case that the cluster solute content dropped by 40%. The effect on the apparent size is more complex to evaluate because it is strongly anisotropic, due to the anisotropy of the resolution in the lateral and evaporation directions. It is clear, however, that these effects are most severe for the smaller clusters, so that particular

care should be taken when interpreting apparent size and compositions of clusters from APT measurements of naturally age-hardened or underaged conditions of Al–Zn–Mg aluminum alloys.

Availability of Data and Materials

The raw data used to reproduce the presented results are available in the Zenodo repository: http://doi.org/10.5281/zenodo.8403644.

Acknowledgments

The Research Council of Norway (RCN) is acknowledged for funding the NTNU atom probe facility. The RCN is further acknowledged for the support to the Norwegian Micro- and Nano-Fabrication Facility, NorFab. The STEM work was conducted on the NORTEM infrastructure (NFR:197405) at the TEM Gemini Centre, Trondheim, Norway.

Financial Support

The current study hasn't received any fund from any organizations or institutions.

Conflict of Interest

The authors declare that they have no competing interest.

References

(2022). Atom Probe Tomography (APT)—Department of Materials Science and Engineering—NTNU.

Danoix F, Miller M & Bigot A (2001). Analysis conditions of an industrial Al–Mg–Si alloy by conventional and 3D atom probes. *Ultramicroscopy* **89**(1–3), 177–188. https://doi.org/10.1016/S0304-3991(01)00098-5

De Geuser F & Gault B (2020). Metrology of small particles and solute clusters by atom probe tomography. *Acta Mater* **188**, 406–415. https://doi.org/10.1016/j.actamat.2020.02.023

De Geuser F, Lefebvre W & Blavette D (2006). 3D atom probe study of solute atoms clustering during natural ageing and pre-ageing of an Al-Mg-Si alloy. *Philos Mag Lett* **86**(4), 227–234. https://doi.org/10.1080/09500830600643270

Engdahl T, Hansen V, Warren P & Stiller K (2002). Investigation of fine scale precipitates in Al–Zn–Mg alloys after various heat treatments. *Mat Sci Eng A* **327**(1), 59–64. https://doi.org/10.1016/S0921-5093(01)01876-7

Famelton J, Hughes G, Williams C, Barbatti C, Moody M & Bagot P (2021). Xenon plasma focussed ion beam preparation of an Al-6XXX alloy sample for atom probe tomography including analysis of an α-Al (Fe. Mn) Si dispersoid. *Mater Charact* **178**, 111194. https://doi.org/10.1016/j.matchar.2021.111194

Felfer P, Ceguerra A, Ringer S & Cairney J (2015). Detecting and extracting clusters in atom probe data: A simple, automated method using Voronoi cells. *Ultramicroscopy* **150**, 30–36. https://doi.org/10.1016/j.ultramic.2014.11.015

Gault B, Moody MP, Cairney JM & Ringer SP (2012). *Atom Probe Microscopy*, pp. 160. Springer Science & Business Media.

Gault B, Moody MP, De Geuser F, Tsafnat G, La Fontaine A, Stephenson LT, Haley D & Ringer SP (2009). Advances in the calibration of atom probe tomographic reconstruction. *J Appl Phys* **105**(3), 034913–1. https://doi.org/10.1063/1.3068197

Geuser FD & Lefebvre W (2011). Determination of matrix composition based on solute-solute nearest-neighbor distances in atom probe tomography. *Microsc Res Tech* **74**(3), 257–263. https://doi.org/10.1002/jemt.20899

Guinier A, Fournet G & Yudowitch KL (1955). *Small-Angle Scattering of X-Rays*.

Hatzoglou C, Klaes B, Delaroche F, Da Costa G, Geiser B, Kühbach M, Wells PB & Vurpillot F (2023). Mesoscopic modeling of field evaporation on atom probe tomography. *J Phys D Appl Phys* **56**(37), 375301. https://doi.org/10.1088/1361-6463/acd649

Hatzoglou C, Radiguet B, Vurpillot F & Pareige P (2018). A chemical composition correction model for nanoclusters observed by APT-application to ODS steel nanoparticles. *J Nucl Mater* **505**, 240–248. https://doi.org/10.1016/j.jnucmat.2018.03.057

Hatzoglou C, Rouland S, Radiguet B, Etienne A, Costa GD, Sauvage X, Pareige P & Vurpillot F (2020). Preferential evaporation in atom probe tomography: An analytical approach. *Microsc Microanal* **26**(4), 689–698. https://doi.org/10.1017/S1431927620001749

Hyde JM, DaCosta G, Hatzoglou C, Weekes H, Radiguet B, Styman PD, Vurpillot F, Pareige C, Etienne A & Bonny G (2017). Analysis of radiation damage in light water reactors: Comparison of cluster analysis methods for the analysis of atom probe data. *Microsc Microanal* **23**(2), 366–375. https://doi.org/10.1017/S1431927616012678

Hyde JM, Marquis E, Wilford K & Williams T (2011). A sensitivity analysis of the maximum separation method for the characterisation of solute clusters. *Ultramicroscopy* **111**(6), 440–447. https://doi.org/10.1016/j.ultramic.2010.12.015

Ivanov R, Deschamps A & De Geuser F (2017). A combined characterization of clusters in naturally aged Al–Cu–(Li, Mg) alloys using small-angle neutron and X-ray scattering and atom probe tomography. *J Appl Crystallogr* **50**(6), 1725–1734. https://doi.org/10.1107/S1600576717014443

Jin S, Su H, Qian F, Li Y & Sha G (2022). Effects of atom probe analysis parameters on composition measurement of precipitates in an Al-Mg-Si-Cu alloy. *Ultramicroscopy* **235**, 113495. https://doi.org/10.1016/j.ultramic.2022.113495

Johnson CA & Klotz JH (1974). The atom probe and Markov chain statistics of clustering. *Technometrics* **16**(4), 483–493. https://doi.org/10.1080/00401706.1974.10489229

Karnesky RA, Sudbrack CK & Seidman DN (2007). Best-fit ellipsoids of atom-probe tomographic data to study coalescence of gamma prime (L1_2) precipitates in Ni-Al-Cr. *Scr Mater* **57**(4), 353–356.

Kelly TF & Miller MK (2007). Atom probe tomography. *Rev sci instrum* **78**(3), 031101. https://doi.org/10.1063/1.2709758

Kruglov T (2005). Correlation function of the excluded volume. *J Appl Crystallogr* **38**(5), 716–720. https://doi.org/10.1107/S0021889805017000

Lawitzki R, Stender P & Schmitz G (2021). Compensating local magnifications in atom probe tomography for accurate analysis of nano-sized precipitates. *Microsc Microanal* **27**(3), 499–510. https://doi.org/10.1017/S1431927621000180

Lefebvre W, Danoix F, Da Costa G, De Geuser F, Hallem H, Deschamps A & Dumont M (2007). 3DAP measurements of Al content in different types of precipitates in aluminium alloys. *Surf Interface Anal* **39**(2-3), 206–212.

Lefebvre W, Philippe T & Vurpillot F (2011). Application of Delaunay tessellation for the characterization of solute-rich clusters in atom probe tomography. *Ultramicroscopy* **111**(3), 200–206. https://doi.org/10.1016/j.ultramic.2010.11.034

Lefebvre W, Vurpillot F & Sauvage X (2016). *Atom Probe Tomography: Put Theory into Practice*. Academic Press.

Lervik A, Thronsen E, Friis J, Marioara CD, Wenner S, Bendo A, Matsuda K, Holmestad R & Andersen SJ (2021). Atomic structure of solute clusters in Al–Zn–Mg alloys. *Acta Mater* **205**, 116574. https://doi.org/10.1016/j.actamat.2020.116574

London AJ, Lozano-Perez S, Moody M, Amirthapandian S, Panigrahi B, Sundar C & Grovenor C (2015). Quantification of oxide particle composition in model oxide dispersion strengthened steel alloys. *Ultramicroscopy* **159**, 360–367. https://doi.org/10.1016/j.ultramic.2015.02.013

Marquis EA & Vurpillot F (2008). Chromatic aberrations in the field evaporation behavior of small precipitates. *Microsc Microanal* **14**(6), 561–570. https://doi.org/10.1017/S1431927608080793

Medrano S, Zhao H, De Geuser F, Gault B, Stephenson L, Deschamps A, Ponge D, Raabe D & Sinclair CW (2018). Cluster hardening in Al-3Mg triggered by small Cu additions. *Acta Mater* **161**, 12–20. https://doi.org/10.1016/j.actamat.2018.08.050

Miller M & Forbes R (2014). *Atom-Probe Tomography: The Local Electrode Atom Probe*. Springer.

Miller M & Kenik E (2004). Atom probe tomography: A technique for nanoscale characterization. *Microsc Microanal* **10**(3), 336–341. https://doi.org/10.1017/S1431927604040577

Philippe T, De Geuser F, Duguay S, Lefebvre W, Cojocaru-Mirédin O, Da Costa G & Blavette D (2009). Clustering and nearest neighbour distances in atom-probe tomography. *Ultramicroscopy* **109**(10), 1304–1309. https://doi.org/10.1016/j.ultramic.2009.06.007

Samudrala S, Wodo O, Suram S, Broderick S, Rajan K & Ganapathysubramanian B (2013). A graph-theoretic approach for characterization of precipitates from atom probe tomography data. *Comput Mater Sci* **77**, 335–342. https://doi.org/10.1016/j.commatsci.2013.04.038

Saxey D (2011). Correlated ion analysis and the interpretation of atom probe mass spectra. *Ultramicroscopy* **111**(6), 473–479. https://doi.org/10.1016/j.ultramic.2010.11.021

Shah S, Gopal A, Thronsen E, Hatzoglou C & Holmedal B (2022*a*). Precipitation, mechanical properties and early slant ductile fracture in cyclic and naturally aged Al-Zn-Mg (-Cu) alloys. *Mater Des* **222**, 111026. https://doi.org/10.1016/j.matdes.2022.111026

Shah S, Thronsen E, Hatzoglou C, Wenner S, Marioara CD, Holmestad R & Holmedal B (2022*b*). Effect of cyclic ageing on the early-stage clustering in Al–Zn–Mg (-Cu) alloys. *Mater Sci Eng A* **846**, 143280.

Stephenson LT, Moody MP, Liddicoat PV & Ringer SP (2007). New techniques for the analysis of fine-scaled clustering phenomena within atom probe tomography (APT) data. *Microsc Microanal* **13**(6), 448–463. https://doi.org/10.1017/S1431927607070900

Stiller K, Warren P, Hansen V, Angenete J & Gjønnes J (1999). Investigation of precipitation in an Al–Zn–Mg alloy after two-step ageing treatment at 100 and 150 C. *Mater Sci Eng A* **270**(1), 55–63. https://doi.org/10.1016/S0921-5093(99)00231-2

Sudbrack CK, Noebe RD & Seidman DN (2006). Direct observations of nucleation in a nondilute multicomponent alloy. *Phys Rev B* **73**(21), 212101. https://doi.org/10.1103/PhysRevB.73.212101

Thronsen E, Shah S, Hatzoglou C, Marioara C, Wenner S, Andersen SJ, Holmedal B & Holmestad R (2023). The evolution of precipitates in an Al–Zn–Mg alloy. *J Mater Res Technol* **23**, 5666–5680. https://doi.org/10.1016/j.jmrt.2023.02.144

Vaumousse D, Cerezo A & Warren P (2003). A procedure for quantification of precipitate microstructures from three-dimensional atom probe data. *Ultramicroscopy* **95**, 215–221. https://doi.org/10.1016/S0304-3991(02)00319-4

Vurpillot F, Bostel A & Blavette D (2000). Trajectory overlaps and local magnification in three-dimensional atom probe. *Appl Phys Lett* **76**(21), 3127–3129. https://doi.org/10.1063/1.126545

Vurpillot F & Oberdorfer C (2015). Modeling atom probe tomography: A review. *Ultramicroscopy* **159**, 202–216. https://doi.org/10.1016/j.ultramic.2014.12.013

Williams CA, Haley D, Marquis EA, Smith GD & Moody MP (2013). Defining clusters in APT reconstructions of ODS steels. *Ultramicroscopy* **132**, 271–278. https://doi.org/10.1016/j.ultramic.2012.12.011

Zelenty J, Dahl A, Hyde J, Smith GD & Moody MP (2017). Detecting clusters in atom probe data with Gaussian mixture models. *Microsc Microanal* **23**(2), 269–278. https://doi.org/10.1017/S1431927617000320

Zhao H, Gault B, Ponge D, Raabe D & De Geuser F (2018). Parameter free quantitative analysis of atom probe data by correlation functions: Application to the precipitation in Al-Zn-Mg-Cu. *Scr Mater* **154**, 106–110. https://doi.org/10.1016/j.scriptamat.2018.05.024